Dynamical mass ejection from the merger of asymmetric binary neutron stars: Radiation-hydrodynamics study in general relativity

Yuichiro Sekiguchi,[1] Kenta Kiuchi,[2] Koutarou Kyutoku,[3] Masaru Shibata,[2] and Keisuke Taniguchi[4]

[1]*Department of Physics, Toho University, Funabashi, Chiba 274-8510, Japan*
[2]*Center for Gravitational Physics, Yukawa Institute for Theoretical Physics, Kyoto University, Kyoto 606-8502, Japan*
[3]*Interdisciplinary Theoretical Science (iTHES) Research Group, RIKEN, Wako, Saitama 351-0198, Japan*
[4]*Department of Physics, University of the Ryukyus, Nishihara, Okinawa 903-0213, Japan*

(Received 6 March 2016; published 17 June 2016)

We perform neutrino radiation-hydrodynamics simulations for the merger of asymmetric binary neutron stars in numerical relativity. Neutron stars are modeled by soft and moderately stiff finite-temperature equations of state (EOS). We find that the properties of the dynamical ejecta such as the total mass, neutron richness profile, and specific entropy profile depend on the mass ratio of the binary systems for a given EOS in a unique manner. For a soft EOS (SFHo), the total ejecta mass depends weakly on the mass ratio, but the average of electron number per baryon (Y_e) and specific entropy (s) of the ejecta decreases significantly with the increase of the degree of mass asymmetry. For a stiff EOS (DD2), with the increase of the mass asymmetry degree, the total ejecta mass significantly increases while the average of Y_e and s moderately decreases. We find again that only for the SFHo, the total ejecta mass exceeds $0.01M_\odot$ irrespective of the mass ratio chosen in this paper. The ejecta have a variety of electron number per baryon with an average approximately between $Y_e \sim 0.2$ and ~ 0.3 irrespective of the EOS employed, which is well suited for the production of the rapid neutron capture process heavy elements (second and third peaks), although its averaged value decreases with the increase of the degree of mass asymmetry.

DOI: 10.1103/PhysRevD.93.124046

I. INTRODUCTION

The merger of binary neutron stars is one of the most promising sources of gravitational waves for ground-based advanced detectors, such as advanced LIGO, advanced VIRGO, and KAGRA [1]. Among them, advanced LIGO already started the first observational run and has achieved the first direct detection of gravitational waves, which were emitted from a binary-black-hole merger [2]. We should expect that these gravitational-wave detectors will also detect the signals of gravitational waves from binary-neutron-star mergers in a few years, because the latest statistical studies suggest that these gravitational-wave detectors will observe gravitational waves from merger events as frequently as $\sim$1–100/yr if the designed sensitivity is achieved [3–5].

Binary-neutron-star mergers are also attracting attention as one of the major nucleosynthesis sites of heavy elements produced by the rapid neutron capture process (r process) [6], because a significant fraction of the neutron-rich matter is likely to be ejected during the merger (see Ref. [7] for the pioneering work). Associated with the production of the neutron-rich heavy elements in the matter ejected during the merger, a strong electromagnetic emission could be induced by the subsequent radioactive decay of the r-process heavy elements [8–10]. This will be an electromagnetic counterpart of gravitational waves from binary-neutron-star mergers and its detection could be used to verify the binary-neutron-star-merger scenario for the r-process nucleosynthesis. This hypothesis is encouraged in particular by the observation of an infrared transient event associated with a short-hard gamma-ray burst, GRB 130603B [11]. These facts strongly encourage the community of gravitational-wave astronomy to theoretically explore the mass ejection mechanisms, the r-process nucleosynthesis in the ejecta, and associated electromagnetic emission in the mergers of binary neutron stars.

For the quantitative study of these topics, we have to clarify the merger process, subsequent mass ejection, physical condition of the ejecta, nucleosynthesis and subsequent decay of the heavy elements in the ejecta, and electromagnetic emission from the ejecta. For these issues, a numerical-relativity simulation, taking into account the detailed microphysical processes and neutrino radiation transfer, is the unique approach. In our previous paper [12], we reported our first numerical-relativity results for these issues focusing only on the equal-mass binaries. We found that the total mass of the dynamically ejected matter during the merger depends strongly on the equations of state (EOS) we employ (see also Refs. [13,14] for the original finding), while the ejecta components have a wide variety of electron number per baryon (denoted by Y_e) between $\approx$0.05 and $\approx$0.5 irrespective of the EOS employed (see also Refs. [15–18] for the follow-up works). The broad Y_e distribution is well suited for explaining the abundance patterns for the r-process heavy elements with the mass

number larger than ∼90 observed in the solar system and ultra metal-poor stars [19].

In this article, we extend our previous study focusing on the merger of asymmetric binary neutron stars: We report our latest numerical results for unequal-mass binary systems of typical neutron-star mass (between 1.25 and $1.45M_\odot$) for a soft EOS (SFHo) [20] and a moderately stiff EOS (DD2) [21]. We show that the physical properties of the merger ejecta depend on the degree of mass asymmetry of the system: The ejecta mass varies with the mass ratio for a fixed value of the binary total mass, and the averaged value of Y_e decreases with the increase of the mass asymmetry degree, although Y_e is always broadly distributed irrespective of the mass ratio.

The paper is organized as follows. In Sec. II, we briefly review the formulation and numerical schemes employed in our numerical-relativity simulation, and also summarize the EOS we employ. In Sec. III, we present numerical results focusing on the dynamical mass ejection and properties of the merger remnants. Section IV is devoted to a summary. Throughout this paper, c and G denote the speed of light and the gravitational constant, respectively.

II. METHOD, EOS, INITIAL MODELS, AND GRID SETUP

We solve Einstein's equation by a puncture-Baumgarte-Shapiro-Shibata-Nakamura formalism as before [12,22,23]. The fourth-order finite-differencing scheme is applied to discretize the field equations except for the advection terms for which the lopsided scheme is employed. The radiation-hydrodynamics equations are solved in the same manner as in Ref. [12]: Neutrino radiation transfer is computed in a leakage scheme [24] incorporating Thorne's moment formalism with a closure relation for a free-streaming component [25,26]. For neutrino heating, which could induce a neutrino-driven wind from the merger remnant, absorption on free nucleons is taken into account.

We employ the SFHo [20] and DD2 [21] for the nuclear-matter EOS, which have been derived recently by Hempel and his collaborators. For these EOS, the predicted maximum mass for spherical neutron stars is 2.06 and $2.42M_\odot$, respectively, and larger than the largest accurately measured mass of neutron stars, $\approx 2.0M_\odot$ [27]. The radius of neutron stars with mass $1.35M_\odot$ for them is $R_{1.35} =$ 11.9 km (SFHo) and 13.2 km (DD2), respectively. These radii depend very weakly on the mass as long as it is in a typical neutron-star mass range between 1.2 and $1.5M_\odot$. Thus, we refer to an EOS with $R_{1.35} \leq 12$ km like the SFHo as a soft EOS. The stellar radius plays a key role in determining the merger remnant and the properties of the dynamical ejecta as we already described in our previous paper [12] (see also Refs. [13,14]).

In numerical simulations, we have to follow the ejecta with the typical velocity of $0.2c$, which expand to ∼2000 km in ∼30 ms. To follow the ejecta motion as well as resolve neutron stars and merger remnants, we employ a fixed mesh-refinement algorithm. As in our previous work [12], we prepare nine refinement levels with the varying grid spacing as $\Delta x_l = 2^{9-l}\Delta x_9$ $(l = 1, 2, \ldots, 9)$ and all the refinement levels have the same coordinate origin. Here, Δx_l is the grid spacing for the lth level in Cartesian coordinates. For each level, the computational domain covers the region $[-N\Delta x_l, N\Delta x_l]$ for x and y directions, and $[0, N\Delta x_l]$ for the z direction (the reflection symmetry with respect to the orbital plane located at $z = 0$ is imposed). In the high-resolution run, we assign $N = 285$, $\Delta x_9 = 150$ m (for the SFHo) or 160 m (for the DD2), and utilize $\approx 7,000$ CPUs on the K computer. Thus, the location of outer boundaries along each axis is $L \gtrsim 10^4$ km and matter ejected from the central region never escapes from the computational domain in our simulation time $\lesssim 60$ ms. To check whether the numerical results depend only weakly on the grid resolution, we also performed lower-resolution simulations for several models. For this case, $N = 160$ and $\Delta x_9 = 250$ m (for the SFHo) or 270 m (for the DD2) and we confirm a reasonable convergence (see Sec. III). We note that since good convergence is found for the models shown in Table I, we do not perform the low-resolution runs for all the models. In the following, the figures are plotted using the results of the high-resolution runs.

The choice of the floor density, which has to be put in a dilute-density or vacuum region outside the neutron stars and merger remnant when using the conservative form of hydrodynamics in numerical simulations, is one of the crucial artificial points for accurately exploring the mass ejection during the merger process. In this study, we set the floor density to be 1.67×10^4 g/cm^3. The floor values of Y_e and temperature are 0.47 and 0.1 MeV, respectively. For this case, the artificial floor only weakly affects the quantitative results of the mass ejection if we focus only on the dynamical ejecta for ∼30 ms after the onset of merger. Here, the contamination in mass would be accumulated to be $\sim 10^{-4}M_\odot$ when the ejecta expands to ∼2000 km in our setting of the atmosphere. Such atmosphere matter decelerates the dynamical ejecta, and then, the ejecta mass (mass with an escape velocity) could be slightly underestimated. To avoid the serious damage by this spurious effect, we analyze the ejecta only for 30 ms after the onset of merger, because the typical ejecta velocity is $0.2c$. For a lower-density floor value, the ejecta mass could be larger. Thus, our present results give the lower bound for the ejecta mass.

In our experiments, we also performed simulations with the floor density 2×10^5 g/cm^3. In this case, the inertia of the atmosphere is too high to follow the ejecta motion accurately: The effect of the atmosphere appears on the ejecta at ∼10 ms after the onset of merger, i.e., before the ejecta reaches a free-expansion stage. In particular, for the case in which the ejecta mass is small ($\lesssim 10^{-3}M_\odot$), this artificial effect is serious: For example, the ejecta mass

TABLE I. The parameters and results of the models employed in this study. m_1 and m_2: each mass of binary in isolation. q: mass ratio defined by $m_2/m_1(\leq 1)$. Δx_9: the grid spacing in the finest refinement level. N: the grid number in one positive direction for each refinement level. $M_{\rm ej}$, $\langle Y_e\rangle$, and $V_{\rm ej}$ denote the dynamical ejecta mass, the averaged value of Y_e, and ejecta velocity measured at 30 ms after the onset of merger. $M_{\rm BH}$ and $a_{\rm BH}$ are the mass and dimensionless spin parameter of the remnant black holes, and $M_{\rm torus}$ is the mass of tori surrounding the remnant black holes for the SFHo models. These values are also measured at 30 ms after the onset of merger. Model name follows the EOS, each mass m_2 and m_1, and grid resolution. The equal-mass data are taken from Ref. [12].

Model	(m_1, m_2)	$q = m_2/m_1$	Δx_9 (m)	N	$M_{\rm ej}(10^{-2}M_\odot)$	$\langle Y_e\rangle$	$V_{\rm ej}$	$M_{\rm BH}(M_\odot)$	$a_{\rm BH}$	$M_{\rm torus}(M_\odot)$
SFHo-135-135h (high)	(1.35, 1.35)	1.00	150	285	1.1	0.31	0.22	2.59	0.69	0.05
SFHo-135-135l (low)	(1.35, 1.35)	1.00	250	160	1.3	0.32	0.21	2.60	0.70	0.03
SFHo-133-137h (high)	(1.37, 1.33)	0.97	150	285	0.8	0.30	0.21	2.59	0.67	0.06
SFHo-130-140h (high)	(1.40, 1.30)	0.93	150	285	0.6	0.27	0.20	2.58	0.67	0.09
SFHo-130-140l (low)	(1.40, 1.30)	0.93	250	160	0.6	0.27	0.21	2.58	0.67	0.08
SFHo-125-145h (high)	(1.45, 1.25)	0.86	150	285	1.1	0.18	0.24	2.58	0.66	0.12
SFHo-125-145l (low)	(1.45, 1.25)	0.86	250	160	1.2	0.19	0.23	2.58	0.66	0.11
DD2-135-135h (high)	(1.35, 1.35)	1.00	160	285	0.2	0.30	0.16	···	···	···
DD2-135-135l (low)	(1.35, 1.35)	1.00	270	160	0.2	0.30	0.15	···	···	···
DD2-130-140h (high)	(1.40, 1.30)	0.93	160	285	0.3	0.26	0.18	···	···	···
DD2-125-145h (high)	(1.45, 1.25)	0.86	160	285	0.5	0.20	0.19	···	···	···

steeply decreases with time for such a low-mass ejecta case because the ejecta are decelerated significantly. We find that it is necessary to reduce the floor density much below 10^5 g/cm^3 to follow the ejecta for a sufficiently long time until the ejecta motion approximately relaxes to a free-expansion stage.[1]

We consider binary neutron stars with each mass between 1.25 and $1.45M_\odot$ fixing the total mass to be $2.7M_\odot$. Neutron stars observed in *compact* binary systems typically have the mass ratio between 0.9 and 1.0, and each mass in the range 1.23–$1.45M_\odot$ [28]. Thus, our choice reasonably reflects the observational fact. The initial orbital separation is chosen so that the orbital angular velocity, Ω, satisfies $Gm_0\Omega/c^3 = 0.028$, where m_0 denotes the total mass, i.e., $m_1 + m_2 = 2.7M_\odot$, and m_1 and $m_2(\leq m_1)$ are the mass of each neutron star in isolation. Table I lists the key parameters of our models and simulation setup. We define the mass ratio by $q := m_2/m_1(\leq 1)$.

III. NUMERICAL RESULTS

A. Summary of the merger process

For all the models we employ in our simulations, a massive neutron star (MNS) is first formed after the onset of merger as expected from our previous results [12,29] (see also our earlier papers [30]). The MNS are long lived in the sense that their lifetime is much longer than their dynamical time scale and rotation period $\lesssim$1 ms. The subsequent evolution of the MNS depends on the EOS employed.

[1]Our numerical results for the ejecta mass are much larger than those by Ref. [15] in which simulations are also performed using the SFHo and DD2. We speculate that one of the reasons for this is that our floor density is much smaller than that in Ref. [15], which employs 5×10^5 g/cm^3. See Sec. III B for another reason.

For the models with the SFHo, the MNS with mass $\gtrsim 2.6M_\odot$ is hypermassive (see Refs. [31,32] for the definition of the hypermassive neutron star) because the maximum mass of spherical and rigidly rotating cold neutron stars is only $\approx$2.06 and $\approx 2.45M_\odot$, respectively. These values are smaller than the remnant MNS mass, and as a result, the MNS collapses to a black hole at $\sim$10 ms after the onset of merger irrespective of the mass ratio: The collapse occurs after the angular momentum inside the MNS is redistributed by the gravitational torque associated with the nonaxial symmetric matter distribution or is dissipated by the gravitational-wave emission.

The lifetime of the remnant MNS depends on the mass asymmetry in a nonmonotonic manner. For SFHo-130-140, the lifetime of the remnant MNS is slightly longer than that for SFHo-135-135. The possible reason for this is that the merger occurs earlier because the smaller-mass neutron star is elongated by a tidal field of the heavier companion (i.e., the merger occurs before the orbital angular momentum is less dissipated by the gravitational-wave emission), and hence, the remnant MNS has more angular momentum for the asymmetric binary. However, for SFHo-125-145, the lifetime of the remnant MNS is shorter than that for SFHo-130-140. The possible reason for this is that shock heating effects at the onset of merger for SFHo-125-145 are less important than for SFHo-130-140. As a result, the internal energy (and the thermal pressure) of the remnant MNS for SFHo-125-145 is smaller than that for SFHo-130-140, resulting in the earlier collapse.

The mass and dimensionless spin parameter of the formed black holes are $\approx 2.6M_\odot$ and $\sim$0.65–0.70, respectively, and the remnant black holes are surrounded by a torus with mass $\sim$0.05–$0.1M_\odot$ and with their typical extent in the orbital plane $\sim$100 km (see Table I and Sec. III C for more details). In reality, such a compact torus is expected to be subsequently evolved by a

magneto-viscous process with the typical lifetime $\tau_v \sim (\alpha_v \Omega)^{-1}$, where α_v is the so-called α parameter for viscous hydrodynamics and $\tau_v \sim 10^2\,\mathrm{ms}(\alpha_v/10^{-2})^{-1}$ for $\Omega = O(10^3\ \mathrm{rad/s})$ (see, e.g., Ref. [33]). Thus, for a plausible value of $\alpha_v \sim 0.01$, this system is a candidate for the central engine of short-hard gamma-ray bursts with the duration less than 1 s, like GRB 130603B [11] (see also Sec. III E).

For the DD2 case, none of the formed MNS collapses to a black hole in our simulation time ∼50 ms. This is reasonable because the maximum mass of spherical and rigidly rotating cold neutron stars for the DD2 is high, i.e., ≈ 2.42 and $2.8 M_\odot$, respectively, and hence, the formed hot MNS with mass $\sim 2.6 M_\odot$ are not hypermassive and cannot collapse to a black hole before a substantial fraction of the angular momentum and thermal energy is dissipated or carried away, respectively, by some angular-momentum transport processes and the neutrino emission (for which the cooling time scale is longer than 1 s; e.g., Refs. [23,29]). The hot remnant MNS is expected to be long lived with their lifetime being longer than a few seconds and could be a strong emitter of neutrinos, which can modify the chemical property of the ejecta via the neutrino irradiation process (see Sec. III C).

B. Dynamical mass ejection

Figure 1 plots the evolution of the total rest mass, $M_{\rm ej}$, and the averaged value for the electron number per baryon, $\langle Y_e \rangle$, of the ejecta for the models with the SFHo and DD2 for a variety of mass ratios. Here, $t_{M_{-6}}$ approximately denotes the time at the onset of merger: It denotes the time at which $M_{\rm ej}$ exceeds $10^{-6} M_\odot$. The average of Y_e for the ejecta is defined by

$$\langle Y_e \rangle = \frac{1}{M_{\rm ej}} \int Y_e dM_{\rm ej}. \tag{3.1}$$

We specify the matter as the ejecta if the lower time component of the fluid four velocity, u_t, is smaller than -1 as before [12]. We note that this condition agrees approximately with the condition $hu_t < -1$ where h is the specific enthalpy. The reason for this is that h is close to unity for the ejecta components moving far from the merger remnant located in the central region. In Table I, we also summarize the total rest mass, the averaged value of Y_e, and the averaged velocity of the ejecta, $V_{\rm ej}$, all of which are measured at $t - t_{M_{-6}} \approx 30$ ms. Here, $V_{\rm ej}$ is defined by $\sqrt{2E_{\rm kin}/M_{\rm ej}}$ where $E_{\rm kin}$ is the total kinetic energy of the ejecta.

Figure 1 illustrates that the ejecta mass depends strongly on the EOS employed, as already described in Ref. [12] (see also Refs. [13,14]): For the smaller value of $R_{1.35}$, the ejecta mass is larger (see also Ref. [15]). Figure 1 also shows that for the models with the SFHo, the ejecta mass depends weakly on the binary mass asymmetry, while for those with the DD2, it increases steeply with the increase of the degree of binary mass asymmetry. Our interpretation to this result is as follows: As described in our study of Ref. [13] in which the piecewise polytropic EOS is

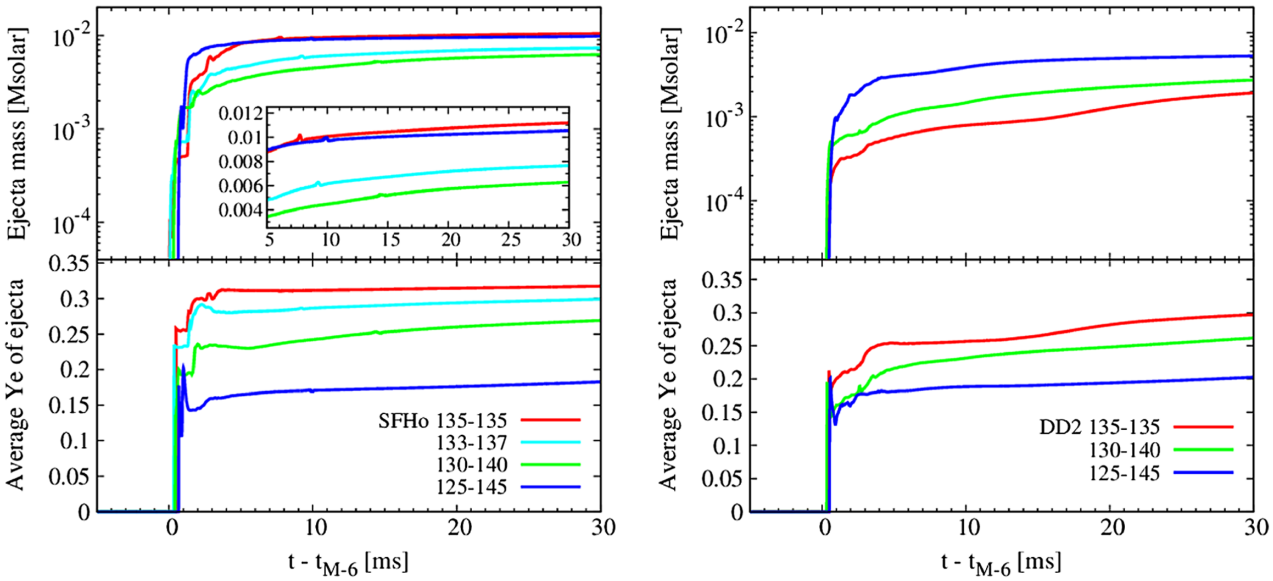

FIG. 1. Rest mass (upper panel) and averaged value of Y_e (lower panel) of the dynamical ejecta as functions of time for the SFHo (left) and DD2 (right) models and for a variety of binary mass ratios. $t_{M_{-6}}$ approximately denotes the time at the onset of merger (see the text). The results for the high-resolution runs are plotted. A substantial fraction of the matter is dynamically ejected at $t - t_{M_{-6}} \lesssim 2$ ms but gradual ejection continues subsequently. The long-term gradual increase of the ejecta mass and the averaged value of Y_e for $t_{M_{-6}} \gtrsim 10$ ms, observed in particular for the DD2 case, is due to the irradiation by neutrons that is emitted from the merger remnant. In the upper left panel, the dynamical ejecta mass in the linear scale for 5 ms $\leq t - t_{M_{-6}} \leq 30$ ms is also shown.

employed, there are two major dynamical mass ejection mechanisms (see also Ref. [14]): shock heating and tidal interaction (i.e., tidal torque exerted by elongated two neutron stars and highly nonaxisymmetric merger remnants). For the equal-mass or slightly asymmetric case, the shock heating should be the primary player of the dynamical mass ejection for neutron stars with soft EOS like the SFHo, while the tidal torque should be the primary player for binary neutron stars with stiff EOS like the DD2. The dependence of the ejecta mass on the EOS stems from this property.

The shock heating efficiency during the merger phase should decrease with the increase of the binary asymmetry degree because the smaller-mass neutron star in such asymmetric systems is tidally elongated just prior to the onset of merger, avoiding the coherent collision with the heavier companion at the merger. Thus, for the models with the SFHo, the shock heating effect should be weakened with the increase of the binary asymmetry degree while the importance of the tidal effect is enhanced (indeed, the maximum temperature of the remnant MNS decreases with the increasing degree of mass asymmetry). As a result of this change in the dynamical mass ejection mechanism, the ejecta mass slightly decreases with the change of q from unity to a smaller value to ~ 0.9. However, with the further decrease of q (i.e., with the further increase of the degree of mass asymmetry), the ejecta mass increases. Our interpretation for this is that the enhanced tidal effect dominates the reduced shock heating effect.

On the other hand, for the DD2 models the tidal interaction is always the primary mechanism for the dynamical mass ejection. The importance of the tidal effect should be further enhanced with the increase of the mass asymmetry degree for this EOS, monotonically increasing the dynamical ejecta mass. Thus, for significantly asymmetric binaries, the typical ejecta mass would approach $10^{-2}M_\odot$ irrespective of the EOS employed. We note that the total ejecta mass depends only weakly on the grid resolution as listed in Table I.

As shown in Fig. 1, the ejecta mass increases steeply with time for the first ~ 10 ms after the onset of merger. This is, in particular, observed for the SFHo models with $q \gtrsim 0.9$ and all the DD2 models. This indicates that we have to follow the ejecta motion at least for ≈ 10 ms after the onset of merger. In a recent simulation of Ref. [15], the authors estimated the properties of the ejecta at $\lesssim 5$ ms after the onset of merger, perhaps because of the small computational domain employed ($L = 750$ km). However, the ejecta mass still increases with time in such an early phase. This could be one of the reasons why our results for the ejecta mass are much larger than theirs. Figure 1 also shows that the average of Y_e still significantly varies with time for the first ~ 5 ms after the onset of merger. This also shows that it would be necessary to determine the properties of the ejecta at $\gtrsim 10$ ms after the onset of merger (if the average of Y_e is estimated at ~ 5 ms after the onset of merger as in Ref. [15], it could be underestimated).

Irrespective of the EOS and mass ratios, the averaged ejecta velocity is in the range between 0.15 and $0.25c$ (see Table I), as found in Refs. [12,13,18]. As we already pointed out in Ref. [13], the ejecta velocity is higher for softer EOS and this indicates that the shock heating effect enhances the ejecta velocity. On the other hand, the ejecta velocity depends only weakly on the mass ratio (as long as it is in the range $0.85 < q \leq 1$), although it is slightly increased for significantly asymmetric binaries like 1.25–$1.45M_\odot$ models.

As described earlier in this section, shock heating and tidal interaction are two major dynamical mass ejection mechanisms. By the tidal torque, the matter tends to be ejected near the orbital plane because the tidal-force vector primarily points in the direction of this plane. On the other hand, by the shock heating, the matter is ejected in a quasispherical manner like in a supernova explosion. Because both effects play a role, the dynamical ejecta usually have a spheroidal morphology [13].

For the SFHo models, the shock heating plays a primary role for the equal-mass or slightly asymmetric case, and hence, the dynamical ejecta in this case have a quasispherical morphology. However, for the significantly asymmetric case, e.g., with $q \sim 0.85$, the tidal effect becomes appreciable, as already mentioned, and hence, the anisotropy of the dynamical ejecta is enhanced. On the other hand, for the DD2 models, the tidal torque always plays a primary role for the dynamical mass ejection. Thus, with the increase of the binary asymmetry degree, this property is further enhanced, and the anisotropy of the dynamical ejecta morphology is increased. Here, we note that the degree of the anisotropy is correlated with the neutron richness of the dynamical ejecta. The possible reasons for this are that (i) the tidally ejected components are less subject to the thermal weak-interaction reprocess associated with the shock heating preserving the neutron-rich nature of the original neutron-star matter and (ii) the neutrino irradiation is less subject to the matter near the equatorial plane than that near the polar region (see the discussion in Sec. III C).

Six panels of Fig. 2 display the profiles of the electron number per baryon, Y_e (left side of each panel), and specific entropy, s (right side of each panel), of the ejecta on the x-y and x-z planes for the SFHo (top panels) and DD2 (lower panels) models. For the SFHo and DD2 models, the snapshots at $t - t_{M_{-6}} \approx 13$ and 10 ms are plotted, respectively. The left, middle, and right panels display the results for 1.35–$1.35M_\odot$, 1.30–$1.40M_\odot$, and 1.25–$1.45M_\odot$, respectively. This figure shows a clear dependence of the properties of the dynamical ejecta on the binary asymmetry degree and on the EOS employed as follows.

(I) For the SFHo models, the specific entropy of the ejecta decreases steeply with the increase of

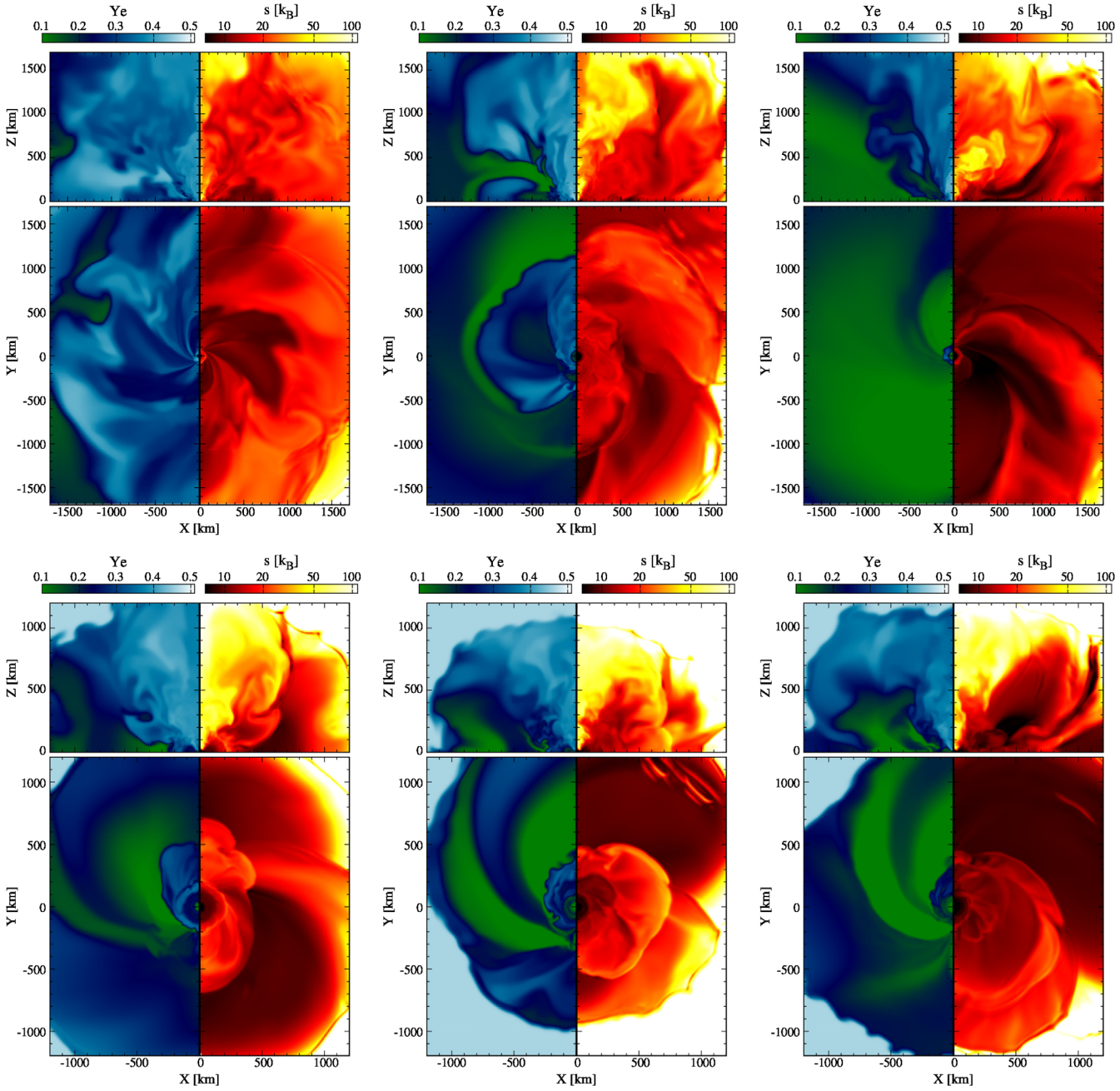

FIG. 2. Profiles of the electron number per baryon, Y_e (left in each panel), and the specific entropy, s (right in each panel), in x-y (lower in each panel) and x-z (upper in each panel) planes. The top three panels show the results for SFHo-135-135h (left), SFHo-130-140h (middle), and SFHo-125-145h (right) at ≈13 ms after the onset of merger. The lower three panels show the results for DD2-135-135h (left), DD2-130-140h (middle), and DD2-125-145h (right) at ≈10 ms after the onset of merger.

the binary asymmetry degree in particular near the orbital plane. Our interpretation for this is that the effect of the shock heating at the onset of the merger, which contributes a lot to the dynamical mass ejection, becomes weak with the increase of the binary asymmetry degree.

(II) As a result, for the SFHo models, the ejecta component with low values of Y_e increases with the increase of the binary asymmetry degree: For the equal-mass case, the ejecta with $Y_e \gtrsim 0.2$ are the primary components while for the 1.25–$1.45M_\odot$ model, those with $Y_e \lesssim 0.2$ are primary (in particular, for the components near the orbital plane). Our interpretation for this is as follows: For a high temperature environment, e^-e^+ pair creation is enhanced, and consequently, the positron capture reaction, $n + e^+ \to p + \bar{\nu}_e$, efficiently proceeds in neutron-rich matter, resulting in the increase of Y_e.

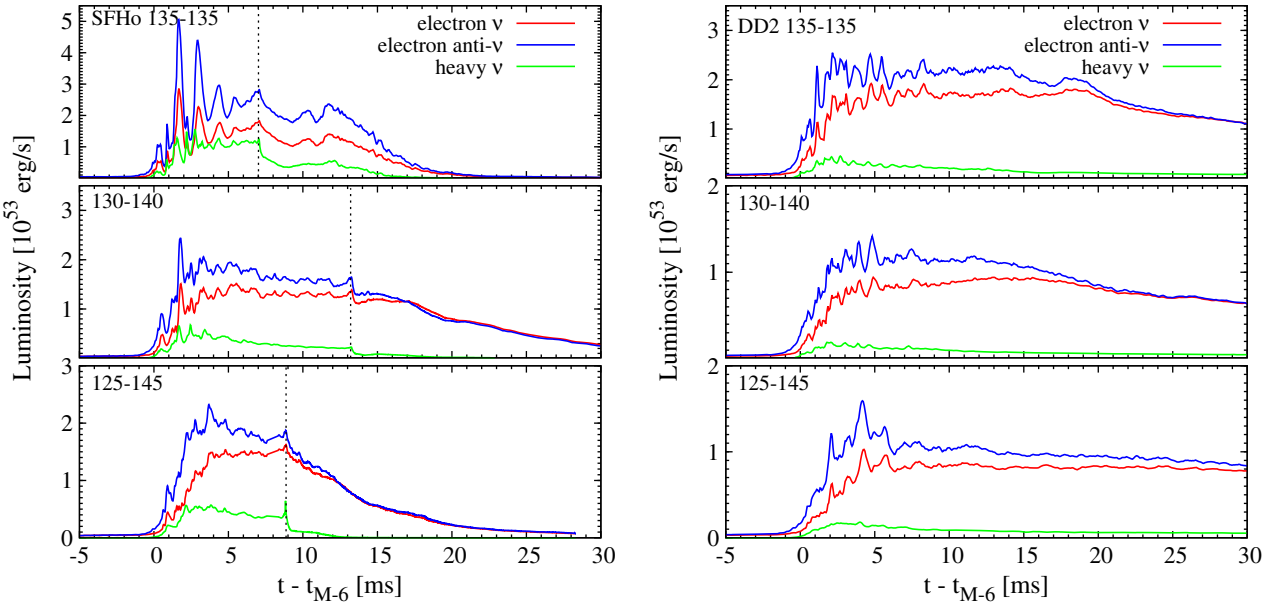

FIG. 3. Luminosity curves of ν_e (red solid), $\bar{\nu}_e$ (blue dashed), and heavy (green dotted-dashed) neutrinos for the models with the SFHo (left) and the DD2 (right), respectively (note that the scales in the vertical axis are different among the plots). For heavy neutrinos, the contribution from only one heavy species is plotted. The vertical dashed lines in the left panel show the time at the formation of a remnant black hole. We note that the relatively high heavy-neutrino luminosity for the SFHo models before the collapse to the remnant black holes reflects the fact that the temperature of remnant MNS is higher and the pair-process neutrino emission is more active than those for the DD2 model.

With the increase of the binary asymmetry degree, the shock heating effect becomes less important and the temperature for a substantial fraction of the dynamical ejecta is decreased. As a result, the positron production and resulting positron capture are suppressed. Hence, the neutron richness is preserved to be relatively high (the value of Y_e is preserved to be low).

(III) For the DD2 models, the effect associated with the binary asymmetry found for the SFHo model is not remarkable: The typical values of Y_e and specific entropy depend mildly on the binary asymmetry degree, although we still observe a monotonic decrease of these values (see, e.g., Fig. 1). This weak dependence is due to the fact that the ejecta are composed primarily of tidally ejected matter irrespective of the mass ratio, as already mentioned.

C. Neutrino irradiation

For the DD2 models, the remnant MNS are long lived, while for the SFHo models, the remnants collapse to a black hole in ∼10 ms after the onset of merger. Therefore, a high-luminosity neutrino emission is continued for a long time scale from the remnant of the DD2 models, while the strong emission continues only briefly for the SFHo models (see Fig. 3). As a result, a long-term neutrino-irradiation effect [12,34–37] plays an important role in heating up the ejecta and increasing the value of Y_e (see the bottom two panels of Fig. 1), in particular, in the region above the remnant MNS pole (see Fig. 2) of the DD2 models.

As we pointed out in Ref. [12], the possible interpretation for the increase of Y_e by the neutrino irradiation is described as follows: The luminosity of electron neutrinos emitted from the remnant hot MNS is quite high as shown in Fig. 3. In such an environment, neutrino capture processes, $n + \nu_e \to p + e^-$ and $p + \bar{\nu}_e \to n + e^+$, could be activated in the matter surrounding the MNS. By the balance of these reactions, the fractions of neutrons and protons are determined and the equilibrium value of Y_e is given by (e.g., Ref. [38])

$$Y_{e,\mathrm{eq}} \sim \left[1 + \frac{L_{\bar{\nu}_e}}{L_{\nu_e}} \cdot \frac{\langle \epsilon_{\bar{\nu}_e} \rangle - 2\Delta}{\langle \epsilon_{\nu_e} \rangle + 2\Delta}\right]^{-1}, \tag{3.2}$$

where $\Delta = m_n c^2 - m_p c^2 \approx 1.293$ MeV, $\langle \epsilon_{\nu_e} \rangle$ and $\langle \epsilon_{\bar{\nu}_e} \rangle$ denote averaged neutrino energy of ν_e and $\bar{\nu}_e$, and L_{ν_e} and $L_{\bar{\nu}_e}$ denote the luminosity of ν_e and $\bar{\nu}_e$, respectively. For the DD2 models, $\langle \epsilon_{\nu_e} \rangle \approx 10$ MeV, $\langle \epsilon_{\bar{\nu}_e} \rangle \approx 15$ MeV, and $L_{\bar{\nu}_e}/L_{\nu_e} \approx 1.0$–$1.3$, and consequently, the expected equilibrium value is $Y_e \approx 0.45$–0.5. This suggests that due to the neutrino irradiation, the neutron richness of the originally neutron-rich matter with $Y_e \lesssim 0.1$ should be decreased (the average of Y_e is increased) towards the equilibrium value.

However, this neutrino irradiation effect depends on the binary asymmetry because, as Fig. 3 shows, the neutrino

luminosity decreases with the increase of the binary asymmetry degree (this is, in particular, seen clearly among the DD2 models). A time scale for the increase of the average value of Y_e may be estimated approximately as (e.g., Ref. [38])

$$\tau_{Y_e} \sim \langle Y_e \rangle \left[\frac{1}{4\pi r^2} \left(\frac{X_n \sigma_{\nu_e n} L_{\nu_e}}{\langle \epsilon_{\nu_e} \rangle} - \frac{X_p \sigma_{\bar{\nu}_e p} L_{\bar{\nu}_e}}{\langle \epsilon_{\bar{\nu}_e} \rangle} \right) \right]^{-1} \sim 40 \text{ ms} \left(\frac{L_\nu}{10^{53} \text{ ergs/s}} \right)^{-1} \left(\frac{r}{100 \text{ km}} \right)^2, \quad (3.3)$$

where r is the coordinate radius; $\sigma_{\nu_e n}$ and $\sigma_{\bar{\nu}_e p}$ are the cross sections of the ν_e absorption on neutrons and $\bar{\nu}_e$ on protons, respectively. Here, we set $\langle \epsilon_{\nu_e} \rangle = 10$ MeV, $\langle \epsilon_{\bar{\nu}_e} \rangle = 15$ MeV, $L_{\nu_e} = L_{\bar{\nu}_e} = L_\nu$, $X_n = 1 - \langle Y_e \rangle$, and $X_p = \langle Y_e \rangle$ with $\langle Y_e \rangle = 0.2$. Thus, for the asymmetric binaries for which L_ν is smaller than that for the equal-mass binary, the time scale to increase Y_e by the neutrino irradiation is longer, as found in Fig. 1: It shows that the rate for the long-term increase in $\langle Y_e \rangle$ is smaller for the more asymmetric binary models.

By this neutrino irradiation, the ejecta mass is also increased (see Fig. 1). This is, in particular, the case for the DD2 models with the equal-mass or weakly asymmetric systems, for which the remnant MNS is long lived and a long-term increase of the ejecta component is observed. For the SFHo models, the MNS is hypermassive and collapses to a black hole in ∼10 ms after the onset of merger, resulting in a significant decrease of the neutrino luminosity. Thus, the effect of the neutrino irradiation is less important irrespective of the binary asymmetry degree.

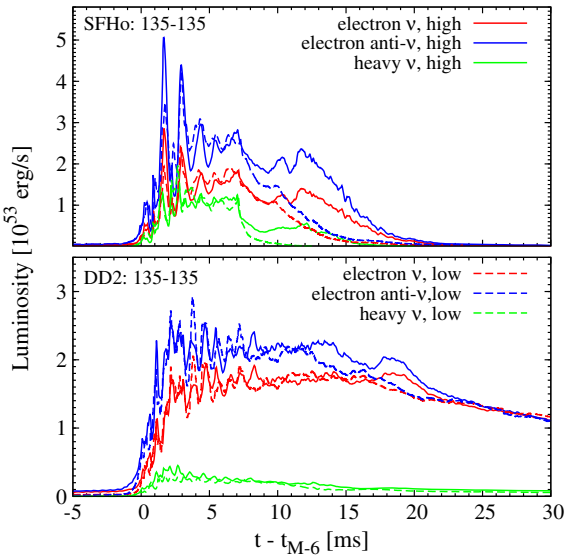

FIG. 4. Dependence of luminosity of ν_e (red), $\bar{\nu}_e$ (blue), and heavy (green) neutrinos on the grid resolution for the SFHo-135-135 (top) and the DD2-135-135 (bottom) models. In each panel, the solid and dashed curves denote the results for the high- and low-resolution runs, respectively.

Figure 4 plots luminosity of ν_e, $\bar{\nu}_e$, and heavy neutrinos with two grid resolutions for SFHo-135-135 and DD2-135-135 models. This illustrates that the luminosity depends only weakly on the grid resolution. For the SFHo models, however, the decay time scale of the neutrino luminosity after the black-hole formation depends on the grid resolution. The reasons for this are that the matter surrounding the formed black hole is smaller for the lower-resolution run perhaps because of larger numerical viscosity (see Table I) and that the compression process of the hot matter surrounding the formed black hole, which forms a disk and primarily emits neutrinos in the black-hole formation phase, depends on the grid resolution: For lower resolutions, the geometrical thickness of the disk is less resolved and the matter temperature is less enhanced, resulting in the lower neutrino luminosity. This grid dependence was also found in the context of a collapsar simulation [39]. Because of this poor-resolution effect, the neutrino irradiation is underestimated. However, this is not a significant effect for the SFHo models, because the ejecta mass is determined primarily by the dynamical mass-ejection phase for $t - t_{M_{-6}} \lesssim 5$ ms and also neutrino luminosity after the black-hole formation is not very high. For the DD2-135-135 model, on the other hand, the magnitude of neutrino luminosity does not depend strongly on the grid resolution because neutrinos are mainly emitted from the well-resolved MNS.

D. Mass distribution of Y_e

The effect of the binary asymmetry is also reflected in the mass distribution of Y_e in an appreciable manner, in particular, for the SFHo models. Figure 5 displays

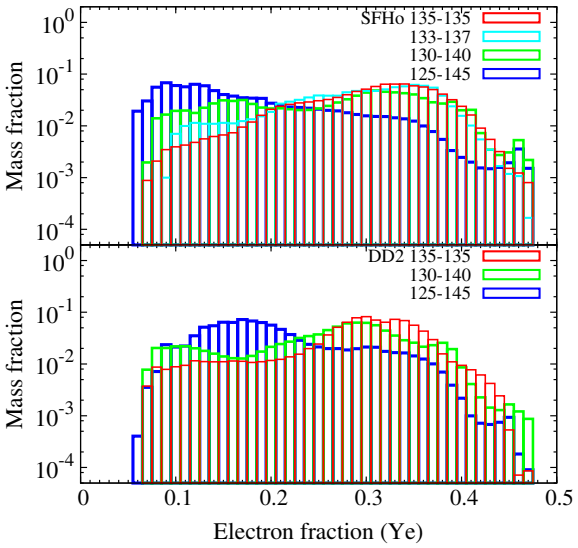

FIG. 5. The mass-distribution histograms with respect to Y_e normalized by the total mass of ejecta for the models with the SFHo (top panel) and DD2 (lower panel), respectively. The data at $t - t_{M_{-6}} \approx 25$ ms are employed.

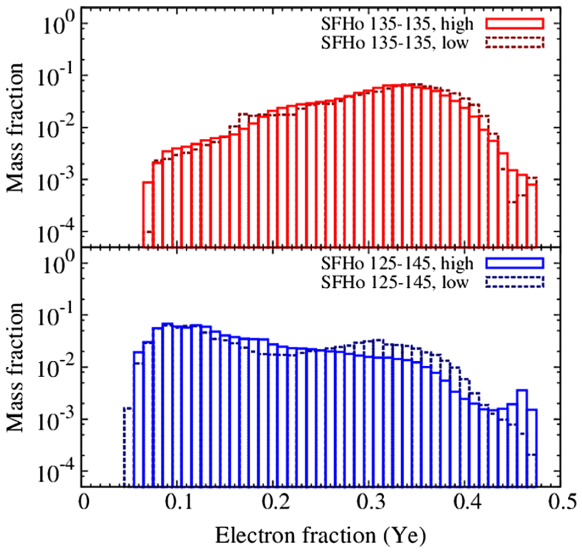

FIG. 6. Dependence of the mass-distribution histograms on the grid resolution for the SFHo-135-135 (top panel) and SFHo-125-145 (lower panel) models, respectively. The solid and dashed lines show the high- and low-resolution results, respectively.

histograms for the ejecta mass fraction as a function of Y_e at $t - t_{M_{-6}} \approx 25$ ms, at which the total (dynamical) ejecta mass and the averaged value of Y_e approximately settle to relaxed values. In Fig. 6, we also display the histograms for two different grid resolutions for the SFHo-135-135 and SFHo-125-145 models to show that they depend only weakly on the grid resolution.

For the equal-mass or slightly asymmetric cases with the SFHo, the ejecta typically have high values of the specific entropy due to strong shock heating at the onset of merger (see Fig. 2). We speculate that as a result of this high value (i.e., the high value of temperature), $e^- e^+$ pair creation is enhanced and subsequently positron capture, $n + e^+ \to p + \bar{\nu}_e$, efficiently proceeds, resulting in the increase of $\langle Y_e \rangle$. Because the shock heating effect for the SFHo models is more significant than that for the DD2 models, the averaged value of Y_e for the ejecta of the SFHo models should be higher than that of the DD2 models for the equal-mass or slightly asymmetric cases (see also Fig. 1).

On the other hand, in the presence of appreciable binary mass asymmetry, not only the shock heating but also the tidal effect become important in the dynamical mass ejection even for the SFHo models. As a result, the fraction of matter with low values of Y_e is increased. This is clearly observed in Fig. 5, which shows that the value of Y_e at the peak gradually shifts to the lower-value side, and in particular, for the 1.25–$1.45 M_\odot$ model, the peak Y_e value is smaller than 0.2 for both the SFHo and DD2 models. However, even in such appreciably asymmetric cases, the dynamical ejecta have a broad distribution in Y_e. This is the universal qualitative feature and well suited for producing a variety of r-process heavy elements [19].

For the 1.25–$1.45 M_\odot$ models, the peak Y_e value for the DD2 model is larger than that for the SFHo model. This trend is different from that for the equal-mass or slightly asymmetric models. The possible reasons for this are that (i) for this significantly asymmetric case, the shock heating effect is not very important and the tidal effect plays a major role in the dynamical mass ejection and (ii) for the DD2 model, the remnant MNS is long lived and the neutrino irradiation plays a more important role than for the SFHo model, resulting in the long-term increase of Y_e for the DD2 model.

E. Properties of the merger remnant

We briefly touch on the properties of the merger remnants located around the central region because the torus around the central merger remnant could be the origin of the further long-term mass ejection (e.g., Refs. [35,36,40]). For the SFHo models, the outcome for $t - t_{M_{-6}} \gtrsim 15$ ms is a rotating black hole surrounded by a massive torus irrespective of the mass ratio, as displayed in Fig. 7. For the SFHo-135-135 model, the torus mass is $\approx 0.05 M_\odot$ and its maximum density is less than 10^{12} g/cm^3. For such relatively low density, the electron degeneracy is not very high and also neutrinos escape efficiently from the torus because the mean free path of neutrinos is as long as or longer than the thickness of the torus.

On the other hand, for the SFHo-125-145 model (also for the SFHo-130-140 model), the torus mass and maximum density are higher than those for the SFHo-135-135 model. In this case the maximum density is higher than $\sim 10^{12}$ g/cm^3, the electron degeneracy is higher than that for the SFHo-135-135 model, and a part of neutrinos is trapped. Then, the β equilibrium among neutrons, protons, electrons, and neutrinos as $n + \nu_e \leftrightarrow p + e^-$ and $p + \bar{\nu}_e \leftrightarrow n + e^+$ is approximately satisfied. Since the electron degeneracy is high, the resulting value of Y_e is lower than that for the SFHo-135-135 model.

Irrespective of the binary mass asymmetry, the resulting compact torus has a high temperature ~ 10 MeV and is cooled dominantly by the neutrino emission. Hence the torus is the neutrino-dominated accretion torus. The order of magnitude for the neutrino luminosity (for ν_e and $\bar{\nu}_e$) is 10^{52} ergs/s (see Fig. 3). Thus, the pair annihilation of neutrinos and antineutrinos to the electron-positron pair, which is not taken into account in our present simulation, would be activated and can modify the dynamics of the merger remnants (e.g., Refs. [41,42]). In addition, the system has a low-density region above the black-hole pole. Such a system satisfies the conditions for the central engine of short-hard gamma-ray bursts.

Massive tori are likely to be subsequently evolved by magnetohydrodynamics (MHD) or viscous processes in reality: Angular momentum inside the tori should then be redistributed and associated with this effect, matter in the tori would be heated up. Then, the geometrical thickness of

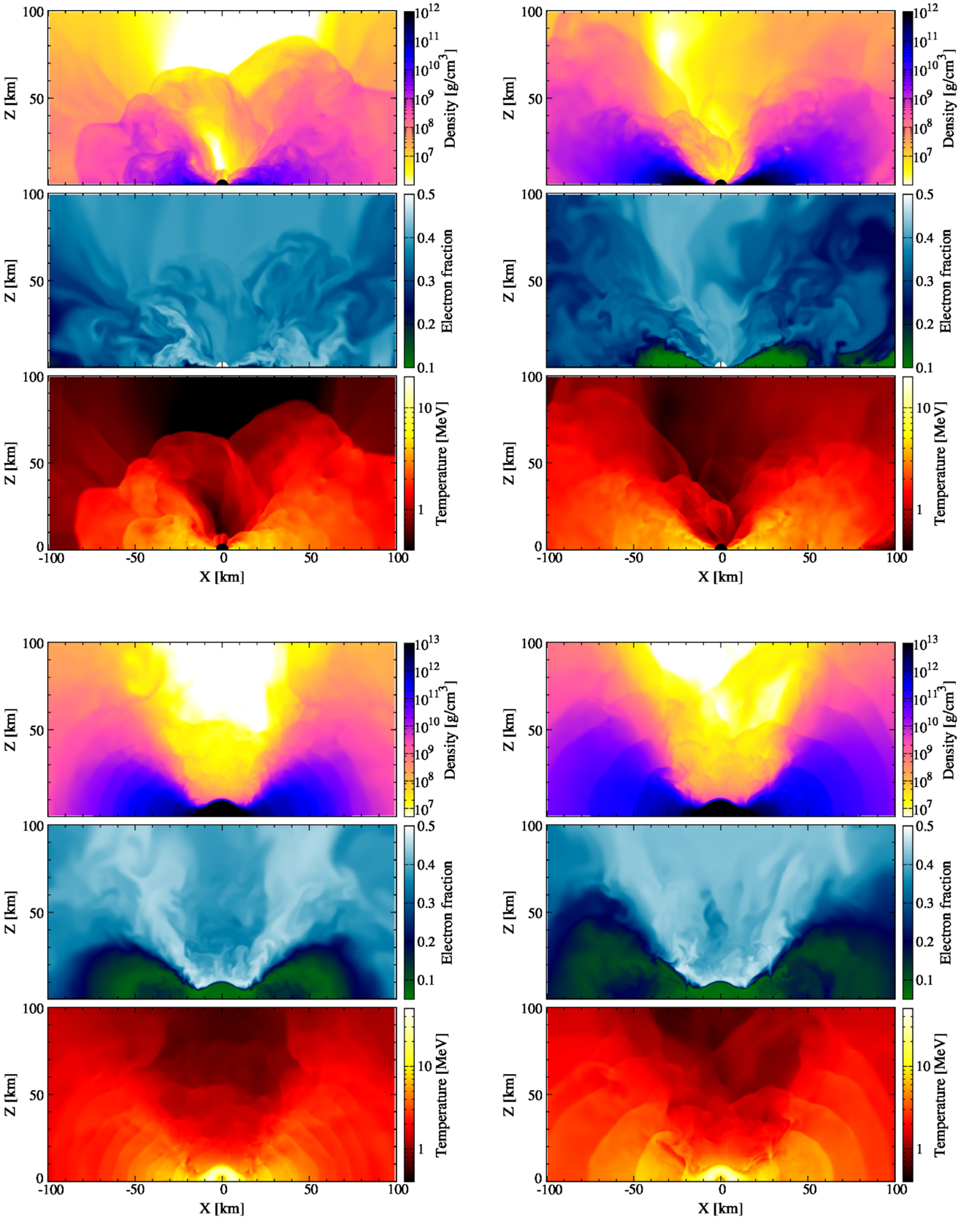

FIG. 7. Profiles of the rest-mass density (top in each panel), electron number per baryon (middle in each panel), and temperature (bottom in each panel) in the *x*-*z* plane for SFHo-135-135h (top left), SFHo-125-145h (top right), DD2-135-135h (bottom left), and DD2-125-145h (bottom right) at 30 ms after the onset of the merger. The filled circles (in black or white) in the top panels denote the inside of black holes.

the tori would be increased, and possibly, an outflow that ejects the matter from the outer part of the tori could be launched [33,35–37,40]. The total rest mass of the ejected matter could reach 10% of the initial torus mass, according to the previous studies. This suggests that the ejecta with mass of the order $0.01M_\odot$ could follow the dynamical mass ejection. We need to explore this process in our future study. On the other hand, the luminosity of neutrinos emitted is not as high as that by the remnant MNS. Thus, neutrino irradiation would not be as important as the MHD/viscous effect for the mass ejection in the black-hole-torus system [36,40].

For the DD2 models, the final outcome is a MNS surrounded by a massive torus as displayed in Fig. 7. Although the central object is different from a black hole, the surrounding matter distribution and velocity profile (close to the Keplerian motion) are similar to those for the SFHo models. Because the density of the MNS and torus is higher than the torus surrounding the black hole found in the SFHo models, the low value of Y_e caused by the electron degeneracy is clearly observed in the DD2 models. As in the torus surrounding black holes, the torus around the MNS is subject to the MHD or viscous effects [37], and hence, it is natural to expect a substantial fraction of mass ejection from the surrounding matter. Because the MNS is long lived for the DD2 models, it is also natural to expect that the neutrino irradiation to the surrounding matter plays an important role in inducing long-term mass ejection.

In the DD2 models, the torus mass and torus extent for the asymmetric binaries are larger than that for the equal-mass one as in the SFHo models. This shows that the binary asymmetry increases not only the dynamical ejecta mass but also the torus mass. This suggests that the mass of the matter ejected by the subsequent MHD/viscous effect is also enhanced in the asymmetric models.

The outer part of the torus surrounding the central object, which is most subject to the mass ejection from the torus, is in general hot and the value of Y_e is not very small ($\gtrsim 0.35$). This suggests that the ejecta are likely to be weakly neutron rich and are less subject to producing the heavy r-process elements, although they could be subject to producing relatively light r-process elements. Exploring the torus-originated components of the ejecta in a self-consistent study from the merger simulation throughout the subsequent remnant evolution is an important issue to fully understand the mass ejection mechanism in the binary-neutron-star merger event. We plan to explore this issue in our future work.

It is interesting to point out that for the DD2 models, the density in the region above the MNS pole is as low as $\lesssim 10^7$ g/cm^3 for $t - t_{M_{-6}} \gtrsim 20$ ms. Since the luminosity of electron neutrinos and antineutrinos emitted from the remnant MNS is high, $\sim 10^{53}$ ergs/s, for the DD2 models, the $\nu_e\bar{\nu}_e$ pair annihilation is expected to be active near the MNS. According to a simple order of magnitude estimate, the pair annihilation luminosity is given by (e.g., Refs. [41,43])

$$L_{\nu_e\bar{\nu}_e} \sim 10^{50}\ \mathrm{ergs/s}\left(\frac{r}{10^7\ \mathrm{cm}}\right)^{-1}\left(\frac{\langle\epsilon_{\nu_e}\rangle + \langle\epsilon_{\bar{\nu}_e}\rangle}{20\ \mathrm{MeV}}\right) \times \left(\frac{L_{\nu_e}}{10^{53}\ \mathrm{ergs/s}}\right)\left(\frac{L_{\bar{\nu}_e}}{10^{53}\ \mathrm{ergs/s}}\right) \times \left(\frac{\cos\Theta}{0.1}\right)^2\left(\frac{\theta_{\mathrm{open}}}{0.1}\right)^{-2}, \quad (3.4)$$

where Θ is the typical angle of the collision between ν_e and $\bar{\nu}_e$; r and θ_{open} denote, respectively, the extent and opening angle above the MNS pole, in which the pair annihilation is enhanced. This luminosity is high enough for launching short-hard gamma-ray bursts like GRB 130603B even for the case in which the merger remnant is surrounded by dynamical ejecta, as demonstrated in Ref. [44]. Because the density of the polar region in the vicinity of the MNS is low, high specific entropy is expected to be achieved in the presence of the $\nu_e\bar{\nu}_e$ pair annihilation. This suggests that a strong outflow or a jet may be launched from this system. If a sufficiently high specific entropy is achieved, a relativistic jet responsible for a short-hard gamma-ray burst can indeed be launched even from the remnant MNS. Including the $\nu_e\bar{\nu}_e$ pair annihilation in our simulation is an important next step.

IV. SUMMARY AND DISCUSSION

We have reported our latest numerical results of neutrino radiation hydrodynamics simulations for binary-neutron-star mergers in general relativity, focusing on the dynamical mass ejection from the merger of asymmetric binary neutron stars with typical mass for each neutron star (1.25–$1.45M_\odot$) and with two representative finite-temperature EOS. The following is the summary of our finding.

(1) The dynamical ejecta mass depends weakly on the mass ratio for the SFHo models. Our interpretation for this is that while the dynamical mass ejection from an equal-mass or nearly equal-mass system is induced primarily by shock heating and this effect becomes weak with the increase of the degree of binary asymmetry, the tidal effect compensates the weakened shock heating effect for the mass ejection in the asymmetric systems.

(2) The dynamical ejecta mass depends significantly on the binary asymmetry degree for the moderately stiff DD2 models; it is $\approx 2 \times 10^{-3}M_\odot$ for the equal-mass case while it is $\approx 5 \times 10^{-3}M_\odot$ for the 1.25–$1.45M_\odot$ model. The reason for this is that the tidal torque, which plays a major role in the dynamical mass ejection in this EOS, is simply enhanced.

(3) The averaged value of Y_e decreases appreciably with the increase of the degree of binary asymmetry irrespective of the EOS employed, and the peak value

of Y_e becomes less than 0.2 for the 1.25–1.45$M_\odot$ models.

(4) Y_e of the ejecta has a broad mass distribution between $\approx$0.05 and $\approx$0.5 irrespective of the EOS and mass ratios. This property is well suited for producing a variety of r-process heavy elements as illustrated in Refs. [18,19].

(5) The neutrino irradiation effect on the dynamical ejecta, which is clearly found for the DD2 models, becomes weak as the binary asymmetry degree increases. Our interpretation for this is that binary asymmetry reduces the shock heating efficiency at the onset of the merger, and as a result, the temperature of the remnant MNS is decreased, reducing the luminosity of the neutrino emission from the MNS.

In our previous papers [12,13], we found for the equal-mass binary merger that the total ejecta mass is larger for softer EOS. It exceeds $0.01M_\odot$ only for the case in which $R_{1.35} \lesssim 12$ km and it is of the order $10^{-3}M_\odot$ for $R_{1.35} > 13$ km. For the case in which the ejecta mass might be of the order $10^{-3}M_\odot$, it may be too small to explain the total mass of *r*-process heavy elements (the so-called second and third-peaks elements) in our Galaxy, unless the galactic merger rate of binary neutron stars is unexpectedly high [45] or some other ejection mechanisms such as the disk wind are present. Our present simulations show that the ejecta mass can be increased in the presence of an appreciable mass asymmetry of the binary systems even for the case in which $R_{1.35} = 13.2$ km. This suggests that even if the EOS is not very soft, the observed total mass of the r-process heavy elements in our Galaxy may be explained in the presence of a substantial fraction of the asymmetric merger events. Here, we stress that even from such asymmetric systems, neutron-rich matter with a variety of Y_e could be ejected.

Nevertheless, if a large fraction of the asymmetric binary merger has a mass ratio of $q \lesssim 0.9$, the averaged value of Y_e is small $\lesssim$0.2 even if the EOS is soft. In such a case, although a substantial amount of the heavy r-process elements around the second and third peaks can be produced, the light elements around the first peak are not significantly produced [18,19]. If this scenario is the case, we may have to rely on other components such as disk-wind components [36,40], which can be produced in the merger remnant for a time scale longer than the dynamical one.

As we mentioned above, the r-process elements are likely to be produced in the neutron-rich ejecta. Because most of the produced r elements are unstable, they subsequently decay and the released energy is the source for an electromagnetic signal, in particular, in the near-infrared optical band [9,10]. Our present study indicates that irrespective of the EOS and mass ratios, the ejecta mass is larger than $10^{-3}M_\odot$. Under this condition, the expected observed magnitude in the near-infrared optical bands is smaller than 24 for an event at 100 Mpc from the earth. Such an event can be observed by Hyper-Suprime Cam (HSC) of the Subaru telescope with one-minute-duration observation [46]. Since HSC (in operation now) can simultaneously observe a field of $\approx$1.75 deg^2, a wide field of $\sim$100 deg^2 can be surveyed in one night by it. Even if the position determination by gravitational-wave detectors is not very good (e.g., Ref. [47]), this wide-field observation will enable us to find a counterpart of the gravitational-wave events. These facts indicate that this radioactively powered electromagnetic signal is the promising electromagnetic counterpart of binary-neutron-star mergers even for the gravitational-wave observation with a small number of detectors (by which the accuracy of the position determination is not very high).

Light curves for this emission have been calculated for the dynamical ejecta [9,10], based on the numerical results for it. In the presence of only the dynamical ejecta, the luminosity simply decreases with time in a power-law manner after the peak luminosity is reached in 1–10 days after the merger (the peak time depends on the wavelength). Here, in the presence of disk-wind components, we have two different types of sources and hence the electromagnetic signals from the ejecta are significantly modified [48].

For the observation of the electromagnetic counterparts, we need a reliable theoretical prediction for the light curves. This is in particular the case for searching the electromagnetic counterparts of short duration. For this issue, we have to take into account all the possible components other than the dynamical ejecta like the disk-wind components. We plan to explore this issue in subsequent works.

ACKNOWLEDGMENTS

We are grateful to M. Hempel for providing the EOS table data and to M. Tanaka for helpful discussion on electromagnetic-counterpart observation. Numerical computations were performed on the supercomputer K at AICS, XC30 at CfCA of NAOJ, FX10 at Information Technology Center of Tokyo University, and SR16000 and XC30 at YITP of Kyoto University. This work was supported by Grant-in-Aid for Scientific Research (Grants No. 24244028, No. 25103510, No. 25105508, No. 24740163, No. 26400267, No. 15K05077, No. 15H06857, No. 15H00783, No. 15H00836, and No. 16H02183), for Scientific Research on Innovative Area (Grant No. 24103001) of Japanese MEXT/JSPS; by HPCI Strategic Program of Japanese MEXT (Project No. hp140211 and No. hp150225); and by a post-K computer priority project (Project No. 9) of Japanese MEXT. Kyutoku was supported by the RIKEN iTHES project.

[1] J. Abadie *et al.*, Nucl. Instrum. Methods Phys. Res., Sect. A **624**, 223 (2010); T. Accadia *et al.*, Classical Quantum Gravity **28**, 025005 (2011); T. Accadia *et al.*, Classical Quantum Gravity **28**, 079501 (2011); K. Kuroda, Classical Quantum Gravity **27**, 084004 (2010).

[2] B. P. Abbott *et al.*, Phys. Rev. Lett. **116**, 061102 (2016).

[3] J. Abadie *et al.* (The LIGO Scientific Collaboration and Virgo Collaboration), Classical Quantum Gravity **27**, 173001 (2010).

[4] M. Dominik, E. Berti, R. O'Shaughnessy, I. Mandel, K. Belczynski, C. Fryer, D. Holz, T. Bulik, and F. Pannarale, Astrophys. J. **806**, 263 (2015).

[5] C. Kim, B. B. P. Perera, and M. A. McLaughlin, Mon. Not. R. Astron. Soc. **448**, 928 (2015).

[6] J. M. Lattimer and D. N. Schramm, Astrophys. J. **192**, L145 (1974).

[7] C. Freiburghaus, S. Rosswog, and F.-K. Thielemann, Astrophys. J. **525**, L121 (1998); S. Rosswog, M. Liebendoerfer, F.-K. Thielemann, M. B. Davies, W. Benz, and T. Piran, Astron. Astrophys. **341**, 499 (1999); S. Rosswog, M. B. Davies, F.-K. Thielemann, and T. Piran, Astron. Astrophys. **360**, 171 (2000).

[8] L.-X. Li and B. Paczynski, Astrophys. J. **507**, L59 (1998).

[9] D. Kasen, N. R. Badnell, and J. Barnes, Astrophys. J. **774**, 25 (2013); J. Barnes and D. Kasen, Astrophys. J. **775**, 18 (2013).

[10] M. Tanaka and K. Hotokezaka, Astrophys. J. **775**, 113 (2013).

[11] N. R. Tanvir, A. J. Levan, A. S. Fruchter, J. Hjorth, R. A. Hounsell, K. Wiersema, and R. L. Tunnicliffe, Nature (London) **500**, 547 (2013); E. Berger, W. Fong, and R. Chornock, Astrophys. J. **774**, L23 (2013).

[12] Y. Sekiguchi, K. Kiuchi, K. Kyutoku, and M. Shibata, Phys. Rev. D **91**, 064059 (2015).

[13] K. Hotokezaka, K. Kiuchi, K. Kyutoku, H. Okawa, Y. Sekiguchi, M. Shibata, and K. Taniguchi, Phys. Rev. D **87**, 024001 (2013).

[14] A. Bauswein, S. Goriely, and H.-T. Janka, Astrophys. J. **773**, 78 (2013).

[15] C. Palenzuela, S. L. Liebling, D. Neilsen, L. Lehner, O. L. Caballero, E. O'Connor, and M. Anderson, Phys. Rev. D **92**, 044045 (2015); L. Lehner, S. L. Liebling, C. Palenzuela, O. L. Caballero, E. O'Connor, M. Anderson, and D. Neilsen, arXiv:1603.00501.

[16] F. Foucart, R. Haas, M. D. Duez, E. O'Connor, C. D. Ott, L. Roberts, L. E. Kidder, J. Lippuner, H. P. Pfeiffer, and M. A. Scheel, Phys. Rev. D **93**, 044019 (2016).

[17] S. Bernuzzi, D. Radice, C. D. Ott, L. F. Roberts, P. Moesta, and F. Galeazzi, arXiv:1512.06397.

[18] D. Radice, F. Galeazzi, J. Lippuner, L. F. Roberts, C. D. Ott, and L. Rezzolla, arXiv:1601.02426.

[19] S. Wanajo, Y. Sekiguchi, N. Nishimura, K. Kiuchi, K. Kyutoku, and M. Shibata, Astrophys. J. Lett. **789**, L39 (2014).

[20] A. Steiner, M. Hempel, and T. Fischer, Astrophys. J. **774**, 17 (2013).

[21] S. Banik, M. Hempel, and D. Bandyophadyay, Astrophys. J. Suppl. Ser. **214**, 22 (2014).

[22] M. Shibata and T. Nakamura, Phys. Rev. D **52**, 5428 (1995); T. W. Baumgarte and S. L. Shapiro, Phys. Rev. D **59**, 024007 (1998); M. Campanelli, C. O. Lousto, P. Marronetti, and Y. Zlochower, Phys. Rev. Lett. **96**, 111101 (2006); J. G. Baker, J. Centrella, D.-I. Choi, M. Koppitz, and J. van Meter, Phys. Rev. Lett. **96**, 111102 (2006).

[23] Y. Sekiguchi, K. Kiuchi, K. Kyutoku, and M. Shibata, Phys. Rev. Lett. **107**, 051102 (2011); Y. Sekiguchi, K. Kiuchi, K. Kyutoku, and M. Shibata, *ibid.* **107**, 211101 (2011).

[24] Y. Sekiguchi, K. Kiuchi, K. Kyutoku, and M. Shibata, Prog. Theor. Exp. Phys. **01**, A304 (2012).

[25] K. S. Thorne, Mon. Not. R. Astron. Soc. **194**, 439 (1981).

[26] M. Shibata, K. Kiuchi, Y. Sekiguchi, and Y. Suwa, Prog. Theor. Phys. **125**, 1255 (2011).

[27] P. Demorest, T. Pennucci, S. Ransom, M. Roberts, and J. Hessels, Nature (London) **467**, 1081 (2010); J. Antoniadis, P. C. C. Freire, N. Wex, T. M. Tauris, R. S. Lynch, M. H. van Kerkwijk, M. Kramer, C. Bassa *et al.*, Science **340**, 1233232 (2013).

[28] For example, D. R. Lorimer, Living Rev. Relativ. **11**, 8 (2008).

[29] K. Hotokezaka, K. Kiuchi, K. Kyutoku, T. Muranushi, Y.-i. Sekiguchi, M. Shibata, and K. Taniguchi, Phys. Rev. D **88**, 044026 (2013).

[30] M. Shibata, K. Taniguchi, and K. Uryū, Phys. Rev. D **71**, 084021 (2005); M. Shibata and K. Taniguchi, Phys. Rev. D **73**, 064027 (2006).

[31] T. W. Baumgarte, S. L. Shapiro, and M. Shiabta, Astrophys. J. Lett. **528**, L28 (2000).

[32] M. Shibata, *Numerical Relavitity* (World Scientific, Singapore, 2016).

[33] K. Kiuchi, K. Kyutoku, Y. Sekiguchi, M. Shibata, and T. Wada, Phys. Rev. D **90**, 041502 (2014); K. Kiuchi, Y. Sekiguchi, K. Kyutoku, M. Shibata, K. Taniguchi, and T. Wada, Phys. Rev. D **92**, 064034 (2015).

[34] L. Dessart, C. D. Ott, A. Burrows, S. Rosswog, and E. Livne, Astrophys. J. **690**, 1681 (2009).

[35] A. Perego, S. Rosswog, R. Cabezon, O. Korobkin, R. Kaeppeli, A. Arcones, and M. Liebendoerfer, Mon. Not. R. Astron. Soc. **443**, 3134 (2014).

[36] O. Just, A. Bauswein, R. A. Pulpillo, S. Goriely, and H.-Th. Janka, Mon. Not. R. Astron. Soc. **448**, 541 (2015).

[37] D. Martin, A. Perego, A. Arcones, F.-K. Thielemann, O. Korobkin, and S. Rosswog, Astrophys. J. **813**, 2 (2015).

[38] Y.-Z. Qian and S. E. Woosley, Astrophys. J. **471**, 331 (1996).

[39] Y. Sekiguchi and M. Shibata, Astrophys. J. **737**, 6 (2011).

[40] R. Fernández and B. Metzger, Mon. Not. R. Astron. Soc. **435**, 502 (2013).

[41] L. Zalamea and A. M. Beloborodov, Mon. Not. R. Astron. Soc. **410**, 2302 (2011).

[42] O. Just, M. Obergaulinger, H.-T. Janka, A. Bauswein, and N. Schwarz, Astrophys. J. Lett. **816**, L30 (2016).

[43] J. Cooperstein, L. J. van den Horn, and E. Baron, Astrophys. J. Lett. **321**, L129 (1987); H.-Th. Janka, Astron. Astrophys. **244**, 378 (1991).

[44] H. Nagakura, K. Hotokezaka, Y. Sekiguchi, M. Shibata, and K. Ioka, Astrophys. J. Lett. **784**, L28 (2014).

[45] K. Hotokezaka, T. Piran, and M. Paul, Nat. Phys. **11**, 1042 (2015).

[46] M. Tanaka (private communication).

[47] S. Nissanke, M. M. Kasliwal, and A. Georgieva, Astrophys. J. **767**, 124 (2013); M. M. Kasliwal and S. Nissanke, Astrophys. J. **789**, L5 (2014).

[48] D. Kasen, R. Fernández, and B. D. Metzger, Mon. Not. R. Astron. Soc. **450**, 1777 (2015).